Capacity Decay in $LiNiO_2$: An Atomistic Kinetic Picture

Penghao Xiao*,†

†*Department of Physics and Atmospheric Science, Dalhousie University, Halifax, Nova Scotia, Canada B3H 4R2*

‡*Department of Chemistry, Dalhousie University, Halifax, Nova Scotia, Canada B3H 4R2*

E-mail: Penghao.Xiao@dal.ca

Abstract

High-Ni layered oxides experience significant capacity decay over cycling, but the underlying mechanisms remain controversial. Using atomistic simulations, the electrochemical behavior of the fatigue phase is reproduced: a surface densified phase traps the last 25% of Li the end of charge, while discharge remains unimpeded. When the Li content falls to 25%, the remaining Li are locked into a superlattice, making the creation of vacancies the rate-limiting step for further delithiation. After cycling, the surface densified phase resembles Ni_5O_8, with 25% Ni in the Li layer forming a similar superlattice. These Ni pin nearby Li, suppressing vacancy formation at the surface and kinetically trapping Li inside. Meanwhile, the Ni_5O_8 phase exhibits high diffusivity for Li interstitials in the superlattice, which explains the minimal resistance increase during discharge at the same Li content. Further densification leads to a surface phase that hinders both charge and discharge across the entire voltage range.

High-Ni layered oxide cathodes have attracted great interest due to their higher energy density within the electrolyte electrochemical window.[1–6] Additionally, the reduced Co contend lowers raw materials costs and minimizes environmental impact. However, as more

capacity is utilized, capacity decay after cycling becomes more pronounced.[7–10] With increasing Ni content, the two-phase character from $LiNiO_2$ emerges at the end of charge: one is the H3 phase containing almost no Li, and the other is the H2 phase containing 25% Li ($Li_{0.25}NiO_2$).[11–17] Abrupt changes, such as Li layer collapse and surface reactivity increase, occur during the H2 to H3 phase transition. Cathode capacity decay primarily occurs in the Li-depleted state; lowering the upper voltage cutoff to avoid the formation of the H3 phase has been shown to greatly improve capacity retention.[8,18–21] It has been reported that surface oxygen evolution is a major contributor to the capacity decay, particularly in single crystals where cracking is largely suppressed and losing contact with the current collector is avoided.[8,22–27] After oxygen loss, dangling transition metals diffuse back into the Li layer, forming rock-salt-like or spinel-like surface phases.[28–31] These surface phases are generally believed to increase the charge/discharge resistance. However, the quantitative relationship between surface phase structure and capacity fade remains unclear. A thorough understanding of this relationship is crucial for maximizing the cycle life and energy density of high-Ni oxides. The insights will also help rationalize surface protection strategies.[32–38]

Previous DFT and TEM studies have shown that the surface densified phase with open Li diffusion channels could be the β phase of composition Ni_5O_8, or the γ phase of composition Ni_3O_4.[31,39,40] Regarding the electrochemical performance after surface densification, Xu et al. observed the formation of a fatigue phase in $LiNi_{0.8}Mn_{0.1}Co_{0.1}O_2$ (NMC811) based on lattice parameter changes, where 25% Li is trapped at the end of charge.[30] The trapping of Li in the fatigue phase has been attributed to the lattice mismatch between the surface phase and the H3 phase. The surface phase's layer spacing does not collapse due to the high concentration of Ni in the Li layer. It was argued that the surface phase pins the Li layer spacing, thereby preventing the delithiation reaction that would otherwise trigger Li layer collapse.[30] However, the H2 and H3 phases can coexist within a single particle despite the significant difference in layer spacing.[41] Since H3 can grow from H2, and H2 is compatible with the surface phase, the reason why H3 cannot coexist with the surface phase becomes

less clear. Ikeda et al. found that capacity decay in $LiNiO_2$ only occurs above 4.1 V and attributed it to the movement of Ni to tetrahedral sites.[42] Bautista Quisbert et al. later reported a gradual shrinkage of the 4.2 V plateau in $LiNiO_2$.[43] Their GITT measurements indicated that the charge overpotential increases dramatically above 4.2 V as capacity fades, while the discharge overpotential at the same Li content remains low. This charge-discharge asymmetry suggests that kinetics plays an important role. Pei et al. recently demonstrated that Al doping in NMC811 helps mitigate the fatigue behavior. While surface densification was alleviated following Al doping, the root cause was attributed to the lattice strain.[35]

In this paper, an alternative explanation for the capacity decay is provided based on atomistic kinetic simulations. With the β phase (Ni_5O_8) on the surface, both the 25% Li trapping at the end of charge and the low overpotential of discharge are reproduced in the simulation. The same effect also causes the high-voltage capacity loss without significant resistance increase at other states of charge (SOC). The β phase traps 25% Li by preventing the H3 phase nucleation from the surface. At the β-H2 interface in the Li layer, immobile Ni from the β phase pin nearby Li from the H2 phase, thus reducing the probability of forming mobile Li. When high energy Li (interstitial with respect to the H2 ordering) is present, they can diffuse quickly through the β phase. Finally, the implications for surface modification strategies are discussed.

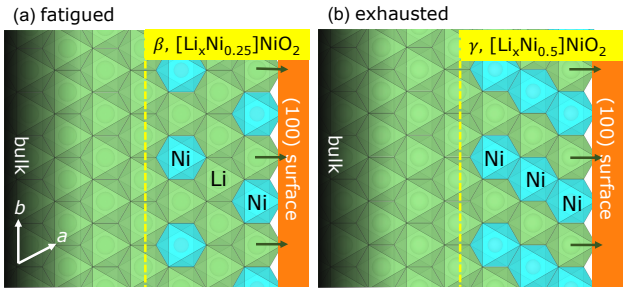

Figure 1: Structure models for (a) fatigued and (b) exhausted cathode particles, showing surface Ni occupancies in the Li layer. Green octahedra are Li; cyan octahedra are Ni in the Li layer. The regions to the right of the yellow dashed lines representing the surface phases, which are (a) β and (b) γ, with compositions of $[Li_xNi_{0.25}]NiO_2$ and $[Li_xNi_{0.5}]NiO_2$, respectively. The dark green arrows indicate the directions of Li extraction.

Model Setup. The two candidate surface phases can be rewritten as $[Ni_{0.25}]NiO_2$ (β) and $[Ni_{0.5}]NiO_2$ (γ), where the composition in the Li layer is indicated in brackets. These two phases are kinetically stable; a higher Ni content in the Li layer will drive fast Ni diffusion into the NiO_2 core and grow the β or γ phase thicker.[39] Figure 1 illustrates models representing cycled particles at two degradation levels: (a) (100) surface is covered with the less densified β phase; (b) (100) surface is covered with the more densified γ phase. Figure 1 (a) and (b) will be referred to as the "fatigued" particle and "exhausted" particle, respectively. In the β phase, Ni occupy every other site forming a 2×2 superlattice, similar to the Li arrangement in the H2 phase. In the γ phase, Ni occupy every other row, resembling the Li ordering in the monoclinic phase. The γ phase occurs in two additional orientations with nearly equal probabilities: one orientation has Ni lines parallel to the a axis, equivalent to Figure 1 (b), while the other has Ni lines parallel to the b axis, which completely blocks Li transport. Consequently, the simulated charge/discharge rate for the exhausted particle should be rescaled by a factor of $\frac{2}{3}$. The surface phase thicknesses are identical, each consisting of three atomic layers ($\sim$1 nm). Both particles are charged and discharged under constant-current constant-voltage (CCCV) conditions with an upper voltage cutoff of 4.4 V, alongside a pristine particle without any surface phase for reference. All simulations are conducted at 400 K unless otherwise specified. Note that the oxygen lattice is fixed in these simulations, and O1-type stacking fault formation is not accounted for. Also, the current setup aims to provide an upper bound for Li transport behavior (fastest possible) dictated by the densified phases in the sub-surface region, without incorporating explicit surface energetics.

The energetics are based on density functional theory (DFT) calculations with the PBE+U exchange-correlation functional using VASP.[44–50] The effect of lattice strain on the H3 phase is examined with the strongly constrained and appropriately normed (SCAN) functional[51,52] with the van der Waals correction in the rVV10 form.[53] A surrogate lattice Hamiltonian is trained on DFT data using cluster expansion for rapid energy evaluation.[54–58] Time evolution

is driven by the rejection-free kinetic Monte Carlo (KMC) algorithm.[59] The cation hopping barriers are dynamically updated based on the local environments through the Brønsted–Evans–Polanyi (BEP) relation.[60–63] The simulation box contains $32 \times 32 \times 8$ O3-type layered $LiNiO_2$ primitive cells ($\sim$ 9.6 nm $\times$ 9.6 nm $\times$ 4.8 nm, 8192 Li sites).[64] More computational details can be found in the Supplementary Information.

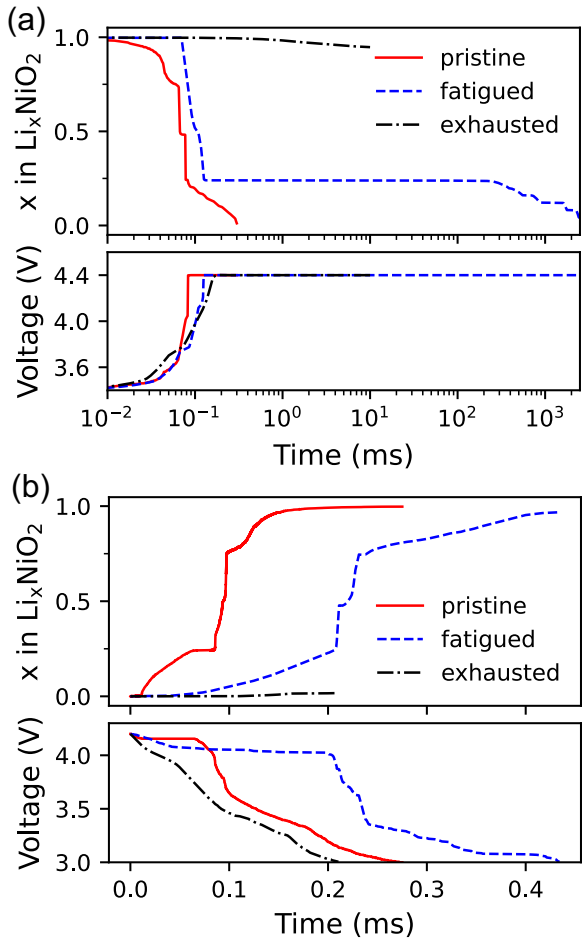

Figure 2: Li fraction (x) in Li_xNiO_2 and voltage as a function of time (a) during charge starting from x = 1 and (b) discharge starting from x = 0. Results for pristine, fatigued, and exhausted particles are compared. The shaded area shows the range of the data from five independent runs.

Simulated charge/discharge time. The Li content and voltage over time for the three particles are plotted together in Figure 2. Figure 2 (a) shows the charge results. Compared to the pristine particle, the fatigued particle begins delithiation at a slightly higher voltage

but proceeds at a similar rate. A major deviation appears when the Li content, x, drops to 0.25 and below. Both particles reach 4.4 V in voltage. The fatigued particle takes 10000 longer to extract the last 25% of Li than the pristine one. There is a long incubation period where x stabilizes at 0.25. This suggests that the last 25% of Li will be kinetically trapped in practice when the surface is covered by the β phase. The above result corroborates Xu et al.'s observation of a bulk fatigue phase with 25% of Li trapped inside at the end of charge after hundreds of cycles.[30] Figure 2 (b) shows the discharge results starting from the fully delithiated structure, NiO_2. For the entire range of x, the discharge time of the fatigued particle is of the same order of magnitude as that of the pristine one. There is no incubation period for $x \leq 0.25$, indicating that the β phase does not impede discharge at high SOC. Experimentally, both Ref 42, 43 reported an overpotential asymmetry between charge and discharge at the highest SOC. Specifically, the overpotential during charge is significantly higher than during discharge at the same Li content. Such asymmetry is persistent with the shrinkage of the highest voltage plateau. Figure 2 (a, b) successfully reproduce this phenomenon from first principles.

In contrast, both the charge and discharge of the exhausted particle in Figure 2 are much slower from the very beginning. Note that the rates must be scaled by $\frac{2}{3}$ to reflect the blocking effects when the Ni lines align parallel to the surface, an orientation that occurs with approximately $\frac{1}{3}$ probability. The γ phase, which forms in more severely degraded particles after prolonged cycling, imposes high resistance to Li transport across all SOC. The presence of γ has been linked to poor electrochemical performance in experiments.[40,65] For the exhausted particle, the amount of trapped Li may exceed 25% due to sluggish kinetics throughout the charge process, which could explain the observation of charged particles stuck at higher Li contents in a recent NMR study.[66]

Atomistic Origin. The different effects of the two surface phases can be understood from the Li-hopping energy landscapes in Figure 3. Conductivity is determined by the product of carrier concentration and mobility (diffusivity). It is important to note that

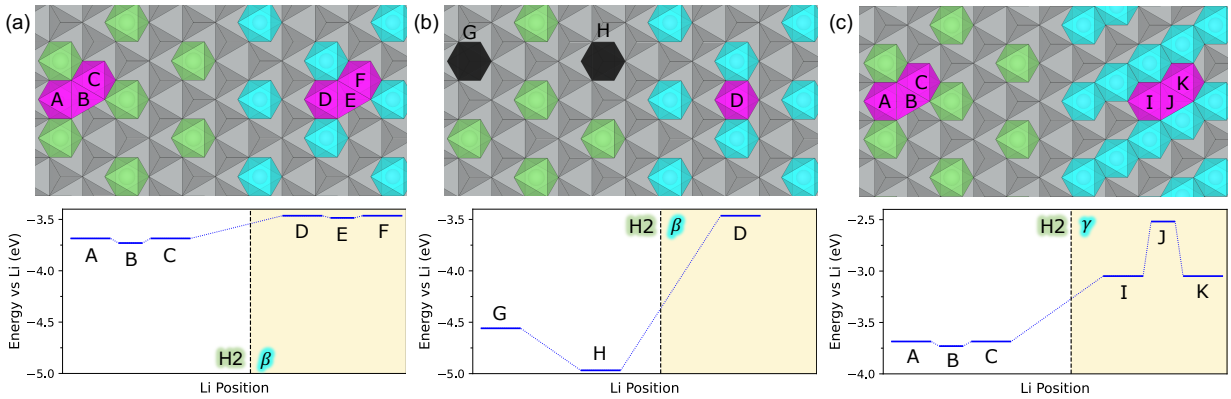

Figure 3: The energy landscapes of a Li hopping through (a) Li interstitial sites (magenta) across H2 and β, (b) vacancy sites (black) in H2 and interstitial sites (magenta) in β, and (c) interstitial sites (magenta) across H2 and γ. The upper panel shows the Li sites: green octahedra are the ordered Li in the H2 phase; cyan octahedra are Ni in the Li layer in the β or γ phase; gray octahedra represent the underlying Ni layer. The lower panel shows the energy levels (relative to Li metal) of a probing Li at each labelled position. The energy difference between an interstitial site and a vacancy site in (b) is the formation energy of an interstitial-vacancy pair.

not all Li are charge carriers, just as not all electrons contribute to electrical conductivity. Figure 3 (a) shows the energy change of an interstitial Li hopping from H2 to β. The β phase forms a coherent interface with the H2 by simply replacing Li with Ni. The energy difference between neighboring tetrahedral and octahedral sites within either H2 or β is less than 0.05 eV (A, B, and C in H2; D, E, and F in β), which gives rise to high Li mobility within each phase. The energy level increases by 0.22 eV moving from C site in H2 to D site in β, driven by stronger Coulombic repulsion from Ni in the Li layer. This introduces a small additional barrier to Li extraction by reducing the concentration of Li in β. In contrast, as shown in Figure 3 (b), when the Li content falls below 25% and no interstitial Li remains in H2, the additional barrier for Li migration from H2 to β increases dramatically. In this case, the formation of an interstitial-vacancy pair (Frenkel defect) is necessary for a Li to migrate into the β phase. Figure 3 (b) shows the energies of Li at vacancy sites in H2 and an interstitial site in β. The interstitial site energy in β remains unchanged from Figure 3 (a), whereas the vacancy site energies in H2 are significantly lower. When a Li hops from site G in H2 (leaving a vacancy behind) to site D in β (forming a Li interstitial), the energy

increases by 1.10 eV; if the Li originates from site H near the H2-β phase boundary, the energy increase is even higher, at 1.50 eV. These energy increases are significantly larger than the 0.85 eV increase when the surface is covered by the H3 phase during charge of the pristine particle.[67] This value decreases further if the vacancy is at the H2-H3 interface, as the Li-Li interactions on one side are disrupted. Forming a single vacancy in H2 is the initial step in nucleating H3. And a vacancy in H2, paired with a Li interstitial in the surface phase (either H3 or β), is an inevitable step for extracting that Li. The β phase stabilizes nearby Li in H2 and destabilizes Li interstitials in β, thereby suppressing the H3 phase nucleation. When the Li content exceeds 25%, there are sufficient interstitials in H2, and the scenario in Figure 3 (a) applies. However, when the Li content drops below 25%, all interstitials are consumed, and the scenario in Figure 3 (b) becomes relevant. Therefore, the β phase does not impede Li extraction in the former case but suppresses the formation of vacancy-interstitial pairs in the latter. This suppression causes the prolonged incubation time observed in the fatigued particle at x = 25% in Figure 2 (a), as vacancy formation in H2 is the critical first step of H3 nucleation during charge.

Figure 4 (a, b) show the 2D top view of a Li layer during the H2-H3 phase transition in the pristine and fatigued particles, respectively. In the pristine particle, the H3 phase grows inwards from the surface; while in the fatigued particle, it grows outwards from the center of the particle. Figure 4 (c, d) show the 3D structure of the remaining Li. The H3 phase expands across all Li layers in both cases, reflecting the strong attraction between Li in neighboring layers.[68,69] In summary, the β phase exhibits high Li mobility/diffusivity, allowing fast Li transport as long as free Li are available to serve as carrier. However, it supresses carrier formation in the H2 phase during charge by sealing the surface and pining nearby Li. During discharge, carriers are injected from outside, so Li transport remains unimpeded by the presence of the β phase.

Compared to the β phase, the γ phase shows reduction in both carrier concentration and mobility. Figure 3 (c) shows the energy change of an interstitial Li hopping from the

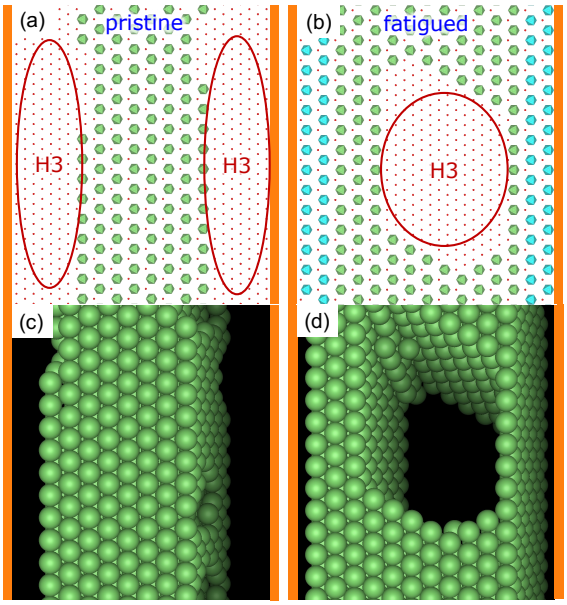

Figure 4: Snapshots at the end of charge showing H3 phase formation in the (a)(c) pristine and (b)(d) fatigued particles. (a) and (b) are 2D views of a single Li layer, with Li in green,Ni in cyan, and unoccupied oxygen lattice marked by red dots; (c) and (d) are 3D views of all layers only showing Li. The H3 phase grows from surface into bulk in the pristine particle but nucleates from bulk in the fatigued particle.

H2 phase to the γ phase. The octahedral site energy increases by 0.64 eV (C-I) from H2 to γ, and the Li hopping barrier within γ is 0.53 eV (I-J). During charge, an interstitial Li hopping through the γ phase must overcome a total barrier of 1.17 eV. During discharge, the carrier concentration can be increased by lowering the voltage, but the low Li mobility remains a persistent issue. The Li hopping barrier in γ is nearly identical to that at the end of discharge for a pristine particle, which leads to first-cycle irreversible capacity loss.[67]

Progress to Fatigue. Oxygen loss and surface densification proceed gradually over cycling, so the densified phase does not cover the whole particle surface at once. Surface coating or doping may also suppress densification in certain regions. Starting from the configuration of Figure 1 (a), where the particle surface is fully covered by the β phase, rows of Ni in the Li layer are randomly removed to represent partially fatigued particles. Figure 5 (a) shows delithiation kinetics of the last 25% capacity at 4.4 V under varying β phase coverages. The general trend is that higher coverage leads to longer incubation time. A

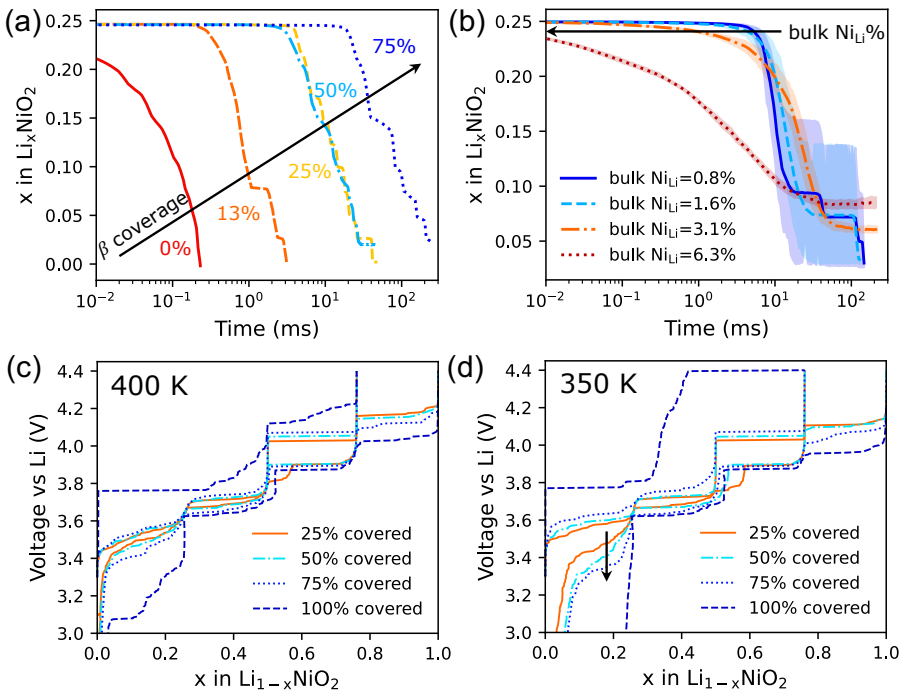

Figure 5: Delithiation time of $Li_{0.25}NiO_2$ with (a) increasing β coverage (black arrow), showing the exponentially increasing incubation time, and (b) increasing bulk Ni_{Li} (black arrow) at 50% β coverage, showing the decreasing incubation time at the constant voltage of 4.4 V (CV hold). The shaded area shows the range of the data from ten runs. Ni_{Li}% in (b) is defined relative to the number of $LiNiO_2$ formula units. (c, d) Constant-current (CC) voltage profiles of $Li_{1-x}NiO_2$, with varying β coverage, between 3.0 and 4.4 V at (c) 400 K and (d) 350 K. The overpotential increase is negligibly small until the β coverage reaches 100%.

13% coverage delays charging by a factor of 10, while 75% coverage slows it by a factor of 1000. In experiments, the voltage-holding time does not span such large orders of magnitude. More sluggish kinetics will result in a higher fraction of trapped Li for a given waiting time, causing progressive capacity loss.

Figure 5 (c) shows corresponding voltage profiles from the constant-current region, where the overpotential growth as a function of β coverage can be seen. Up to 75% β coverage, changes in the voltage profiles remains minimal, despite significant delay developing at 4.4 V (Figure 5 (a)). At 100% coverage, charge overpotential begins to increase, and discharge overpotential rises significantly below 3.6 V. In Figure 5 (d), the temperature is lowered to 350 K to amplify the effects of slow kinetic. The discharge overpotential gradually increases with the coverage below 3.6 V, as indicated by the arrow. This results in the shrinkage of the lowest plateau and capacity loss during discharge. The origin of this behavior is the same as the increased first-cycle irreversible capacity loss observed with higher amount of excess Ni in the bulk.[67] Experimentally, it has also been found that the shrinkage of the 4.2 V plateau has little effect on the rest of the voltage profile in $LiNiO_2$.[42,43] Ref 43 also shows a gradual capacity decay at the end of discharge. Note that the simulations are under the Born-Oppenheimer approximation, which assumes that electrons are always in equilibrium (infinite electrical conductivity). This implies that improving electrical conductivity alone would not resolve the high resistance issue during charge above 4.15 V.[43] Also, no tetrahedral Ni is present in the above simulations, as it does not form without excess Ni in the bulk.[39,67] Therefore, the capacity decay cannot be attributed to tetrahedral Ni either. The simulation associates the progressive capacity decay with β phase coverage, showing that with less than 100% coverage the capacity losses at both ends are moderate. This suggests that mitigating capacity decay does not require full surface protection; partial coating or doping may be sufficient to preserve enough intact surface for H3 phase nucleation.

Excess Ni in the Bulk (Ni_{Li}) refers to Ni located in the Li layer within the bulk material, primarily formed during synthesis as a result of Li evaporation.[70] Figure 5 (b)

shows the delithiation time for the last 25% of Li as a function of Ni_{Li} concentration at 50% β coverage. The initial configurations are obtained by equilibrating structures with specified amounts of Ni_{Li} at 4.1 V for 2×10^6 steps, with all sites directly accessible to the Li reservoir under grand canonical conditions. The equilibrated Li contents are normalized to 0.25 for better comparison. As Ni_{Li} increases, the incubation time spent at x = 0.25 is reduced. At 6.3% Ni_{Li}, the Li content decreases continuously from the start, suggesting that the fatigued particle could be delithiated below 25%. Interestingly, 1.3% Ni_{Li} occupy tetrahedral sites at time 0, which does not appear to significantly impede Li transport compared to the cyan curve in Figure 5 (a) with the same β coverage but no tetrahedral Ni. The presence of Ni_{Li} primarily disrupts Li ordering in H2 and increases the energy of certain Li sites. These high-energy Li are more likely to become interstitials and get extracted, leaving behind vacancies that serve as nucleation sites for the H3 phase. Over longer periods (> 100 ms), higher Ni_{Li} levels results in greater residual Li. These remaining Li are the second-nearest octahedral neighbours of Ni_{Li}, such as site H in Figure 3 (b). Ni_{Li} trap Li at the end of charge in pristine particles for the same reason.[67] Considering that Ni_{Li} also increases the first-cycle capacity loss at the end of discharge, its slight effect on slowing down capacity fade at high voltages offers only marginal benefit. Raising the energy of Li in the H2 phase by doping could be an alternative approach to recover some capacity in fatigued particles.

Lattice Mismatch The simulations above do not include long-range elastic energy from lattice mismatch. It has been suggested that the surface phase suppresses the lattice collapse, thereby preventing H3 phase formation.[30] Since PBE+U cannot capture the lattice collapse of the H3 phase due to the lack of van der Waals interactions, SCAN+rVV10 was used to quantify the lattice pinning effect caused by the surface phase. The calculated equilibrium c lattice parameters are 13.39 Å for the H3 phase and 14.24 Å for the H2 phase, while the experimental values are 13.338 Å and 14.399 Å, respectively.[15] The Li layer spacing of the H3 phase was then fixed to that of the H2 phase to eliminate the change in lattice mismatch between the bulk and surface phases after the H2-H3 phase transition. The energy increase

due to this constraint reflects the energy penalty from the lattice pinning. The resulting charge voltage increases is 0.040 V (0.058 V using experimental c), which accounts for only a small fraction of the overpotential observed.[43] In reality, strain decays to zero far from the interface, so applying this constraint to the entire bulk provides an upper bound for the energy penalty.

In summary, the electrochemical behaviors of the fatigue phase in high Ni layered cathodes are explained by atomistic kinetic simulations from first principles. The surface β phase (Ni_5O_8) is identified as the key factor responsible for trapping the last 25% of Li at the end of charge, while remaining conductive to the other Li. Neither Ni in tetrahedral sites nor lattice strain is a major contributor to this behavior. The β phase strongly anchors nearby Li to the ordered positions in the H2 phase, prohibiting Li vacancy-interstitial pair formation near the surface and thereby hindering H3 phase nucleation. Conversely, it adds minimal resistance to the diffusion of existing Li interstitials. The β phase act as a native passivation layer that prevents further degradation and allow fast transport of high-energy Li. For surface modifications that inhibit surface densification, careful design is needed to ensure that artificial surface phases outperform the β phase. They must exhibit high mobility and high carrier concentration across the entire SOC range. A counterexample is the γ phase (Ni_3O_4), which has open channels yet impedes Li transport. Additionally, not all Li are mobile, and a phase with high Li content does not necessarily have high carrier concentration. A potential strategy could involve combining the naturally formed β phase with partial surface coating or dilute surface doping: the artificial surface provides nucleation sites for H3 phase formation at the end of charge, while the β phase remains conductive across other SOC. Another direction is to disrupt Li ordering in the H2 phase through bulk doping. With the elucidation of the roles of the surface phases, new pathways for further optimization of high-Ni layered oxides could be unlocked.

Supporting Information: Additional computational details, including parameters and settings for DFT, cluster expansion, and KMC; compositions and convex hulls of the training

data.

Acknowledgements

This work was funded by the Natural Sciences and Engineering Research Council of Canada (NSERC) under the Discovery Grant RGPIN-2022-02969. The computational resources were provided by ACENET and the Digital Research Alliance of Canada.

References

(1) Myung, S. T.; Maglia, F.; Park, K. J.; Yoon, C. S.; Lamp, P.; Kim, S. J.; Sun, Y. K. Nickel-Rich Layered Cathode Materials for Automotive Lithium-Ion Batteries: Achievements and Perspectives. *ACS Energy Lett.* **2017**, *2*, 196–223.

(2) Schipper, F.; Erickson, E. M.; Erk, C.; Shin, J.-Y.; Chesneau, F. F.; Aurbach, D. Review—Recent Advances and Remaining Challenges for Lithium Ion Battery Cathodes. *J. Electrochem. Soc.* **2017**, *164*, A6220–A6228.

(3) Li, W.; Erickson, E. M.; Manthiram, A. High-nickel layered oxide cathodes for lithium-based automotive batteries. *Nat. Energy* **2020**, *5*, 26–34.

(4) Liu, T. et al. Understanding Co roles towards developing Co-free Ni-rich cathodes for rechargeable batteries. *Nat. Energy* **2021**, *6*, 277–286.

(5) Liu, Z. D.; Wang, C. Y.; Zhang, J. C.; Luo, J. W.; Zeng, C. H.; Liu, W. D.; Liu, R.; Chen, Y. N. Co-free/Co-poor high-Ni cathode for high energy, stable and low-cost lithium-ion batteries. *Rare Met.* **2023**, *42*, 2214–2225.

(6) Yu, L.; Liu, T.; Amine, R.; Wen, J.; Lu, J.; Amine, K. High Nickel and No Cobalt-The Pursuit of Next-Generation Layered Oxide Cathodes. *ACS Appl. Mater. Interfaces* **2022**, *14*, 23056–23065.

(7) Märker, K.; Reeves, P. J.; Xu, C.; Griffith, K. J.; Grey, C. P. Evolution of Structure and Lithium Dynamics in $LiNi_{0.8}Mn_{0.1}Co_{0.1}O_2$ (NMC811) Cathodes during Electrochemical Cycling. *Chem. Mater.* **2019**, *31*, 2545–2554.

(8) Quilty, C. D.; Luo, J.; Rodriguez-Campos, A.; Liu, S.; West, P. J.; Tong, X.; Kiss, A.; Yang, Y.; Jaye, C.; Fischer, D. A.; Takeuchi, E. S.; Marschilok, A. C.; Bock, D. C.; Yan, S.; Takeuchi, K. J. Capacity Fade of Graphite/NMC811: Influence of Particle Morphology, Electrolyte, and Charge Voltage. *J. Electrochem. Soc.* **2024**, *171*, 080515.

(9) Li, T.; Yuan, X. Z.; Zhang, L.; Song, D.; Shi, K.; Bock, C. Degradation Mechanisms and Mitigation Strategies of Nickel-Rich NMC-Based Lithium-Ion Batteries. *Electrochem. Energy Rev.* **2020**, *3*, 43–80.

(10) Gan, Q.; Qin, N.; Yuan, H.; Lu, L.; Xu, Z.; Lu, Z. Critical review on the degradation mechanisms and recent progress of Ni-rich layered oxide cathodes for lithium-ion batteries. *EnergyChem* **2023**, *5*.

(11) Dahn, J.; Michal, C. Structure and electrochemistry of $Li_{1\pm y}NiO_2$ and a new Li_2NiO_2 phase with the $Ni(OH)_2$ structure. *Solid State Ion.* **1990**, *44*, 87–97.

(12) Dahn, J.; Von Sacken, U.; Juzkow, M.; Al-Janaby, H. Rechargeable $LiNiO_2$/carbon cells. *J. Electrochem. Soc.* **1991**, *138*, 2207.

(13) Reimers, J.; Dahn, J. In situ x-ray diffraction and electrochemical studies of $Li_{1-x}NiO_2$. *Solid State Ion.* **1993**, *67*, 123–130.

(14) Delmas, C.; Peres, J. P.; Rougier, A.; Demourgues, A.; Weill, F.; Chadwick, A.; Broussely, M.; Perton, F.; Biensan, P.; Willmann, P. On the Behavior of The Li_xNiO_2 System: An Electrochemical and Structural Overview. *J. Power Sources* **1997**, *68*, 120–125.

(15) Li, H.; Zhang, N.; Li, J.; Dahn, J. Updating the Structure and Electrochemistry of Li_xNiO_2 for $0 \leq x \leq 1$. *J. Electrochem. Soc.* **2018**, *165*, A2985.

(16) Bianchini, M.; Roca-Ayats, M.; Hartmann, P.; Brezesinski, T.; Janek, J. There and back again—the journey of $LiNiO_2$ as a cathode active material. *Angew. Chem. Int. Ed.* **2019**, *58*, 10434–10458.

(17) Mock, M.; Bianchini, M.; Fauth, F.; Albe, K.; Sicolo, S. Atomistic understanding of the $LiNiO_2$–NiO_2 phase diagram from experimentally guided lattice models. *J. Mater. Chem. A* **2021**, *9*, 14928–14940.

(18) Li, J.; Harlow, J.; Stakheiko, N.; Zhang, N.; Paulsen, J.; Dahn, J. Dependence of Cell Failure on Cut-Off Voltage Ranges and Observation of Kinetic Hindrance in LiNi 0.8 Co 0.15 Al 0.05 O 2. *J. Electrochem. Soc.* **2018**, *165*, A2682–A2695.

(19) Yoon, C. S.; Jun, D.-W.; Myung, S.-T.; Sun, Y.-K. Structural Stability of $LiNiO_2$ Cycled above 4.2 V. *ACS Energy Lett.* **2017**, *2*, 1150–1155.

(20) Eldesoky, A.; Bauer, M.; Bond, T.; Kowalski, N.; Corsten, J.; Rathore, D.; Dressler, R.; Dahn, J. R. Long-Term Study on the Impact of Depth of Discharge, C-Rate, Voltage, and Temperature on the Lifetime of Single-Crystal NMC811/Artificial Graphite Pouch Cells. *J. Electrochem. Soc.* **2022**, *169*, 100531.

(21) Liu, Y.; Song, W.; Eldesoky, A.; Harlow, J.; Logan, E. R.; Li, H.; Dahn, J. R. The Impact of Upper Cut-Off Voltage on the Cycling Performance of Li-Ion Cells with Positive Electrodes Having Various Nickel Contents. *J. Electrochem. Soc.* **2022**, *169*, 040531.

(22) Zhao, W. et al. Quantifying Degradation Parameters of Single-Crystalline Ni-Rich Cathodes in Lithium-Ion Batteries. *Angew. Chem. Int. Ed.* **2023**, *62*.

(23) Lee, S.; Su, L.; Mesnier, A.; Cui, Z.; Manthiram, A. Cracking vs. surface reactivity in high-nickel cathodes for lithium-ion batteries. *Joule* **2023**, *7*, 2430–2444.

(24) Oswald, S.; Gasteiger, H. A. The Structural Stability Limit of Layered Lithium Transition Metal Oxides Due to Oxygen Release at High State of Charge and Its Dependence on the Nickel Content. *J. Electrochem. Soc.* **2023**, *170*, 030506.

(25) Menon, A. S. et al. Quantifying Electrochemical Degradation in Single-Crystalline $LiNi_{0.8}Mn_{0.1}Co_{0.1}O_2$–Graphite Pouch Cells through Operando X-Ray and Postmortem Investigations. *PRX Energy* **2024**, *3*.

(26) Schweidler, S.; Biasi, L. D.; Garcia, G.; Mazilkin, A.; Hartmann, P.; Brezesinski, T.; Janek, J. Investigation into Mechanical Degradation and Fatigue of High-Ni NCM Cathode Material: A Long-Term Cycling Study of Full Cells. *ACS Appl. Energy Mater.* **2019**, *2*, 7375–7384.

(27) Ko, D. S.; Park, J. H.; Yu, B. Y.; Ahn, D.; Kim, K.; Han, H. N.; Jeon, W. S.; Jung, C.; Manthiram, A. Degradation of High-Nickel-Layered Oxide Cathodes from Surface to Bulk: A Comprehensive Structural, Chemical, and Electrical Analysis. *Adv. Energy Mater.* **2020**, *10*.

(28) Lin, F.; Markus, I. M.; Nordlund, D.; Weng, T. C.; Asta, M. D.; Xin, H. L.; Doeff, M. M. Surface reconstruction and chemical evolution of stoichiometric layered cathode materials for lithium-ion batteries. *Nat. Commun.* **2014**, *5*, 3529.

(29) Hwang, S.; Chang, W.; Kim, S. M.; Su, D.; Kim, D. H.; Lee, J. Y.; Chung, K. Y.; Stach, E. A. Investigation of changes in the surface structure of $Li_xNi_{0.8}Co_{0.15}Al_{0.05}O_2$ cathode materials induced by the initial charge. *Chem. Mater.* **2014**, *26*, 1084–1092.

(30) Xu, C.; Märker, K.; Lee, J.; Mahadevegowda, A.; Reeves, P. J.; Day, S. J.; Groh, M. F.; Emge, S. P.; Ducati, C.; Mehdi, B. L.; Tang, C. C.; Grey, C. P. Bulk fatigue induced by surface reconstruction in layered Ni-rich cathodes for Li-ion batteries. *Nat. Mater.* **2021**, *20*, 84–92.

(31) Mukherjee, P.; Lu, P.; Faenza, N.; Pereira, N.; Amatucci, G.; Ceder, G.; Cosandey, F. Atomic Structure of Surface-Densified Phases in Ni-Rich Layered Compounds. *ACS Appl. Mater. Interfaces* **2021**, *13*, 17478–17486.

(32) Riesgo-González, V.; Hall, D. S.; Märker, K.; Slaughter, J.; Wright, D. S.; Grey, C. P. Effect of Annealing on the Structure, Composition, and Electrochemistry of NMC811 Coated with Al2O3 Using an Alkoxide Precursor. *Chem. Mater.* **2022**, *34*, 9722–9735.

(33) Chen, J.; Yang, Y.; Tang, Y.; Wang, Y.; Li, H.; Xiao, X.; Wang, S.; Darma, M. S. D.; Etter, M.; Missyul, A.; Tayal, A.; Knapp, M.; Ehrenberg, H.; Indris, S.; Hua, W. Constructing a Thin Disordered Self-Protective Layer on the $LiNiO_2$ Primary Particles Against Oxygen Release. *Adv. Funct. Mater.* **2023**, *33*.

(34) Konuma, I.; Ikeda, N.; Campéon, B. D.; Fujimura, H.; Kikkawa, J.; Luong, H. D.; Tateyama, Y.; Ugata, Y.; Yonemura, M.; Ishigaki, T.; Aida, T.; Yabuuchi, N. Unified understanding and mitigation of detrimental phase transition in cobalt-free $LiNiO_2$. *Energy Storage Mater.* **2024**, *66*, 103200.

(35) Pei, B.; Zhou, H.; Zong, Y.; Chen, X.; Zuba, M. J.; Zhou, G.; Liu, H.; Whittingham, M. S. Fatigue Phase Suppression in Aged High Nickel Layered Cathodes by Aluminum Substitution during Co-precipitation. *ACS Energy Lett.* **2024**, 3913–3921.

(36) Zhou, T.; Wang, H.; Wang, Y.; Jiao, P.; Hao, Z.; Zhang, K.; Xu, J.; Liu, J. B.; He, Y. S.; Zhang, Y. X.; Chen, L.; Li, L.; Zhang, W.; Ma, Z. F.; Chen, J. Stabilizing lattice oxygen in slightly Li-enriched nickel oxide cathodes toward high-energy batteries. *Chem* **2022**, *8*, 2817–2830.

(37) Rathore, D.; Geng, C.; Zaker, N.; Hamam, I.; Liu, Y.; Xiao, P.; Botton, G. A.; Dahn, J.; Yang, C. Tungsten Infused Grain Boundaries Enabling Universal Performance Enhancement of Co-Free Ni-Rich Cathode Materials. *J. Electrochem. Soc.* **2021**, *168*, 120514.

(38) Su, Y.; Li, L.; Chen, L.; Wang, L.; Lu, Y.; Zhang, Q.; Bao, L.; Wu, F. Enhanced Electrochemical Performance of Ni-Rich Cathode Materials with an In Situ-Formed $LiBO_2/B_2O_3$ Hybrid Coating Layer. *ACS Appl. Energy Mater.* **2022**, *5*, 2231–2241.

(39) Xiao, P.; Shi, T.; Huang, W.; Ceder, G. Understanding surface densified phases in Ni-rich layered compounds. *ACS Energy Lett.* **2019**, *4*, 811–818.

(40) Pan, R.; Jo, E.; Cui, Z.; Manthiram, A. Degradation Pathways of Cobalt-Free $LiNiO_2$ Cathode in Lithium Batteries. *Adv. Funct. Mater.* **2023**, *33*.

(41) Ryu, H. H.; Namkoong, B.; Kim, J. H.; Belharouak, I.; Yoon, C. S.; Sun, Y. K. Capacity Fading Mechanisms in Ni-Rich Single-Crystal NCM Cathodes. *ACS Energy Lett.* **2021**, *6*, 2726–2734.

(42) Ikeda, N.; Konuma, I.; Rajendra, H. B.; Aida, T.; Yabuuchi, N. Why is the O3 to O1 phase transition hindered in $LiNiO_2$ on full delithiation? *J. Mater. Chem. A* **2021**, *9*, 15963–15967.

(43) Quisbert, E. B.; Fauth, F.; Abakumov, A. M.; Blangero, M.; Guignard, M.; Delmas, C. Understanding the High Voltage Behavior of $LiNiO_2$ Through the Electrochemical Properties of the Surface Layer. *Small* **2023**, *19*.

(44) Kresse, G.; Hafner, J. Ab initio molecular dynamics for liquid metals. *Phys. Rev. B* **1993**, *47*, R558–R561.

(45) Kresse, G.; Hafner, J. Ab initio molecular-dynamics simulation of the liquid-metal amorphous-semiconductor transition in germanium. *Phys. Rev. B* **1994**, *49*, 14251–14269.

(46) Perdew, J. P. In *Electronic Structure of Solids*; Ziesche, P., Eschrig, H., Eds.; Akademie Verlag: Berlin, 1991; pp 11–20.

(47) Perdew, J. P.; Burke, K.; Ernzerhof, M. Generalized Gradient Approximation Made Simple. *Phys. Rev. Lett.* **1996**, *77*, 3865.

(48) Dudarev, S.; Botton, G.; Savrasov, S.; Humphreys, C.; Sutton, A. Electron-Energy-Loss Spectra and the Structural Stability of Nickel Oxide: An LSDA+U Study. *Phys. Rev. B* **1998**, *57*, 1505–1509.

(49) Wang, L.; Maxisch, T.; Ceder, G. Oxidation energies of transition metal oxides within the GGA+ U framework. *Phys. Rev. B* **2006**, *73*, 195107.

(50) Das, H.; Urban, A.; Huang, W.; Ceder, G. First-Principles Simulation of the (Li−−Ni−−Vacancy)O Phase Diagram and Its Relevance for the Surface Phases in Ni-Rich Li-Ion Cathode Materials. *Chem. Mater.* **2017**, *29*, 7840–7851.

(51) Sun, J.; Ruzsinszky, A.; Perdew, J. P. Strongly constrained and appropriately normed semilocal density functional. *Phys. Rev. Lett.* **2015**, *115*, 036402.

(52) Sun, J.; Remsing, R. C.; Zhang, Y.; Sun, Z.; Ruzsinszky, A.; Peng, H.; Yang, Z.; Paul, A.; Waghmare, U.; Wu, X.; Klein, M. L.; Perdew, J. P. Accurate first-principles structures and energies of diversely bonded systems from an efficient density functional. *Nat. Chem.* **2016**, *8*, 831.

(53) Peng, H.; Yang, Z.-H.; Perdew, J. P.; Sun, J. Versatile van der Waals density functional based on a meta-generalized gradient approximation. *Phys. Rev. X* **2016**, *6*, 041005.

(54) Sanchez, J. M.; Ducastelle, F.; Gratias, D. Generalized cluster description of multicomponent systems. *Phys. A: Stat. Mech. Appl.* **1984**, *128*, 334–350.

(55) van de Walle, A.; Ceder, G. Automating first-principles phase diagram calculations. *J. Phase Equilibria* **2002**, *23*, 348–359.

(56) Puchala, B.; Van der Ven, A. Thermodynamics of the Zr−O system from first-principles calculations. *Phys. Rev. B* **2013**, *88*, 094108.

(57) Nelson, L. J.; Hart, G. L.; Zhou, F.; Ozoliņš, V. Compressive sensing as a paradigm for building physics models. *Phys. Rev. B* **2013**, *87*, 035125.

(58) Huang, W.; Urban, A.; Rong, Z.; Ding, Z.; Luo, C.; Ceder, G. Construction of ground-state preserving sparse lattice models for predictive materials simulations. *npj Computational Materials* **2017**, *3*, 30.

(59) Voter, A. F. *Radiation Effects in Solids*; Springer Netherlands: Dordrecht, 2007; pp 1–23.

(60) Evans, M.; Polanyi, M. Inertia and driving force of chemical reactions. *Trans. Faraday Soc.* **1938**, *34*, 11–24.

(61) Bronsted, J. Acid and Basic Catalysis. *Chem. Rev.* **1928**, *5*, 231–338.

(62) Bligaard, T.; Nørskov, J. K.; Dahl, S.; Matthiesen, J.; Christensen, C. H.; Sehested, J. The Brønsted–Evans–Polanyi Relation and the Volcano Curve in Heterogeneous Catalysis. *J. Catal.* **2004**, *224*, 206–217.

(63) Xiao, P.; Henkelman, G. Kinetic Monte Carlo Study of Li Intercalation in $LiFePO_4$. *ACS Nano* **2018**, *12*, 844–851.

(64) Delmas, C.; Carlier, D.; Guignard, M. The Layered Oxides in Lithium and Sodium-Ion Batteries: A Solid-State Chemistry Approach. 2021.

(65) Fajardo, G. J. P. et al. Synergistic Degradation Mechanism in Single Crystal Ni-Rich NMC//Graphite Cells. *ACS Energy Lett.* **2023**, *8*, 5025–5031.

(66) Nguyen, H.; Kurzhals, P.; Bianchini, M.; Seidel, K.; Clément, R. J. New insights into aging in $LiNiO_2$ cathodes from high resolution paramagnetic NMR spectroscopy. *Chem. Commun.* **2024**, *60*, 4707–4710.

(67) Xiao, P.; Zhang, N.; Perez, H. S.; Park, M. Atomistic Origins of Asymmetric Charge–Discharge Kinetics in Off-Stoichiometric $LiNiO_2$. *Chem. Mater.* **2024**, *36*, 3296–3306.

(68) Arroyo y de Dompablo, M. E.; Marianetti, C.; Van der Ven, A.; Ceder, G. Jahn-teller mediated ordering in layered Li_xMO_2 compounds. *Phys. Rev. B* **2001**, *63*.

(69) Arroyo y de Dompablo, M.; Van der Ven, A.; Ceder, G. First-principles calculations of lithium ordering and phase stability on Li_xNiO_2. *Phys. Rev. B* **2002**, *66*, 064112.

(70) McCalla, E.; Carey, G.; Dahn, J. Lithium loss mechanisms during synthesis of layered $Li_xNi_{2-x}O_2$ for lithium ion batteries. *Solid State Ion.* **2012**, *219*, 11–19.

supplemental information to Capacity Decay in $LiNiO_2$: An Atomistic Kinetic Picture

Penghao Xiao*

Department of Physics and Atmospheric Science, Dalhousie University, Halifax, Nova Scotia, Canada B3H 4R2

E-mail: Penghao.Xiao@dal.ca

Computational Method

DFT calculation

The density functional theory (DFT) calculations are performed with the Vienna Ab initio Simulation Package (VASP) using the projector augmented wave method and plane wave basis set.[1–5] The generalized-gradient approximation with the Perdew-Burke-Ernzerhof (PBE) functional is used for the exchange-correlation energy.[6,7] The rotationally invariant Hubbard U correction is applied on $3d$ orbitals,[8] with an effective U value of 6.0 eV for Ni.[9–11] The lattice pinning effect is evaluated by the strongly constrained and appropriately normed (SCAN) functional[12,13] with the long-range van der Waals (vdW) interaction in the rVV10 form.[14] The k-point sampling is done on a Γ-centered mesh with a density of 20 Å. The energy cutoff for plane waves is 520 eV.

Cluster expansion

The PBE+U energies are used to train a cluster expansion (CE) model with the CASM code.[15–17] The CE is based on a face-centered-cubic (FCC) oxygen lattice with cations (Li or Ni) on octahedral and tetrahedral sites. The cutoff radii for pairs, triplets and quadruplets are 6, 6, and 4 Å. The L_1-norm regularization with a hyperparameter $\lambda = 0.03$ is applied to select a sparse set of non-zero effective cluster interactions (ECIs).[18] Ground states are preserved during CE fitting by employing quadratic programming.[19] Additionally, points near the convex hull, which are likely to be visited during the kinetic simulation, are assigned greater weights during training. The final CE model has 111 clusters and achieves an overall root-mean-squared error of 11 meV/O (meV per oxygen). The training data distribution in the ternary space and energy comparisons along representative lines are summarized in Figure S1.

Kinetic simulation

The rejection-free KMC is implemented with cations (Li and Ni) hopping between face-sharing octahedral and tetrahedral sites in the oxygen lattice.[20–22] Direct hopping between edge-sharing octahedral sites is not included. For single-vacancy hops, the barrier through the O-O edge is encoded into the nearest tetrahedral site energy. The KMC simulation box contains $32 \times 32 \times 8$ O3-type layered $LiNiO_2$ primitive cells. Periodic boundary conditions are used in all directions. Three consecutive rows of octahedral sites along the (010) direction of the layered structure are treated as grand canonical, enabling Li creation and annihilation to mimic surface behavior, while the remaining sites are canonical to simulate the bulk diffusion.

The hopping rate, r, is evaluated by the Arrhenius equation with the activation barrier, E_a, calculated on the fly based on the Brønsted–Evans–Polanyi (BEP) principle.[23–25] BEP

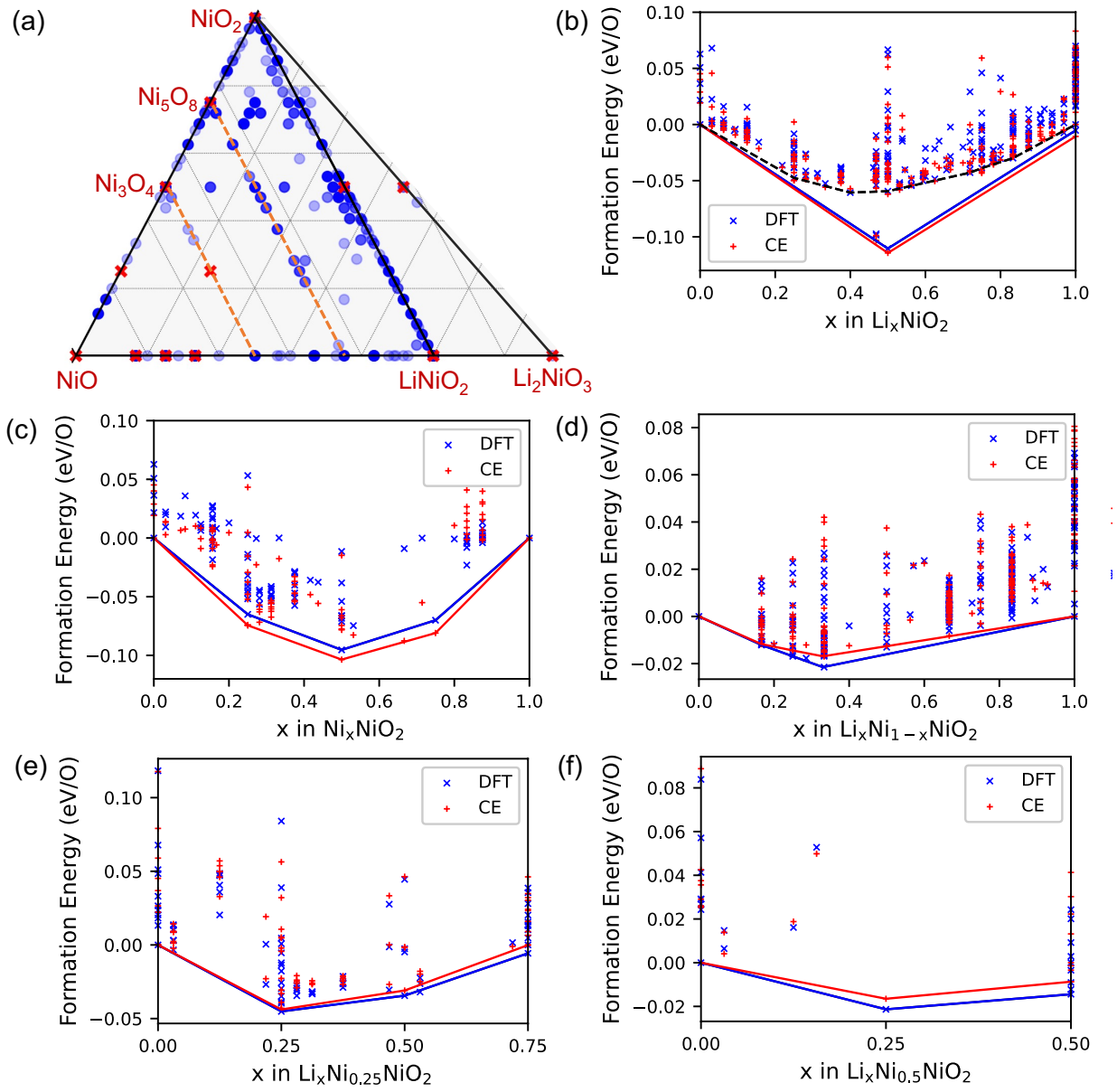

Figure S1: Visualization of the training data in cluster expansion (CE). (a) Compositions of the training data in the $LiNiO_2 - NiO_2 - NiO$ ternary phase space. Red crosses are structures on the convex hull, and blue dots are those above the hull. The darker the blue, the more structures are present for that composition. (b) – (f) Energy comparison between DFT (blue) and CE (red) along representative lines in the phase space. (b) $NiO_2 - LiNiO_2$; (c) $NiO_2 - NiO$; (d) $NiO - LiNiO_2$; (e) $Ni_{0.25}NiO_2 - Li_{0.75}Ni_{0.25}NiO_2$; (f) $Ni_{0.5}NiO_2 - Li_{0.5}Ni_{0.5}NiO_2$. Solid lines outline the convex hulls. Black dashed line in (b) connects the layered structures of the lowest DFT energies (layered hull).

linearly correlates E_a with the energy difference between the two adjacent local minima, ΔE:

$$E_a = E_{a0} + \frac{1}{2}\Delta E \tag{1}$$

$$r = A \exp\left\{\left(\frac{-E_a}{k_B T}\right)\right\} \tag{2}$$

where A is a constant prefactor; E_{a0} is the intrinsic hopping barrier that depends on the ion type; k_B is the Boltzmann constant; T is the temperature. A is set to $10^{13}\,\mathrm{s}^{-1}$, a common approximation for elementary processes in solids.[26] E_{a0} is 0.15 eV for Li and 0.50 eV for Ni, respectively, based on nudged elastic band calculations.[27–29] For grand canonical moves, Eq.2 becomes

$$r = A \exp\left\{\left(\frac{-E_{as}}{k_B T}\right)\right\} \exp\left\{\left(\frac{-0.5(E_i - U)}{k_B T}\right)\right\} \tag{3}$$

where E_i is the Li energy on an adsorbing site; U is the Li energy in the reservoir (anode), which is equal to the negative of voltage v.s. Li metal; E_{as} is the intrinsic barrier for Li attaching/detaching to the electrode. An $E_{as} = 0.3\,\mathrm{eV}$ is chosen for Li to ensure the surface process is not excessively fast to cause numerical inefficiency.

To simulate the galvanostatic scan, the voltage in the surface region is dynamically adjusted based on the current feedback. Specifically, the voltage changes in steps of $\pm$ 5 mV when the current drops below a set threshold. This scheme may result in voltage overshoot for phases with fast Li diffusion, but the error will remain below the 5 mV step size. Charging transitions to constant voltage at 4.4 V, while discharging ends at 3.0 V. The current is determined by linearly fitting the number of remaining Li atoms over time for every 0.5 µs. The threshold current is set to one Li per µs for the given lattice size, corresponding to $0.16\,\mathrm{A/cm^2}$. The absolute current appears high compared to experimental values, but the simulation targets a single particle with a 9.6 nm diffusion length.

References

(1) Kresse, G.; Hafner, J. Ab initio molecular dynamics for liquid metals. *Phys. Rev. B* **1993**, *47*, R558–R561.

(2) Kresse, G.; Hafner, J. Ab initio molecular-dynamics simulation of the liquid-metal amorphous-semiconductor transition in germanium. *Phys. Rev. B* **1994**, *49*, 14251–14269.

(3) Kresse, G.; Joubert, J. From Ultrasoft Pseudopotentials to the Projector Augmented Wave Method. *Phys. Rev. B* **1999**, *59*, 1758.

(4) Kresse, G.; Furthmüller, J. Efficient Iterative Schemes for Ab Initio Total-Energy Calculations Using a Plane-Wave Basis Set. *Phys. Rev. B* **1996**, *54*, 11169–11186.

(5) Kresse, G.; Furthmüller, J. Efficiency of Ab-Initio Total Energy Calculations for Metals and Semiconductors Using a Plane-Wave Basis Set. *Comput. Mater. Sci.* **1996**, *6*, 15–50.

(6) Perdew, J. P. In *Electronic Structure of Solids*; Ziesche, P., Eschrig, H., Eds.; Akademie Verlag: Berlin, 1991; pp 11–20.

(7) Perdew, J. P.; Burke, K.; Ernzerhof, M. Generalized Gradient Approximation Made Simple. *Phys. Rev. Lett.* **1996**, *77*, 3865.

(8) Dudarev, S.; Botton, G.; Savrasov, S.; Humphreys, C.; Sutton, A. Electron-Energy-Loss Spectra and the Structural Stability of Nickel Oxide: An LSDA+U Study. *Phys. Rev. B* **1998**, *57*, 1505–1509.

(9) Wang, L.; Maxisch, T.; Ceder, G. Oxidation energies of transition metal oxides within the GGA+ U framework. *Phys. Rev. B* **2006**, *73*, 195107.

(10) Jain, A.; Hautier, G.; Ong, S. P.; Moore, C. J.; Fischer, C. C.; Persson, K. A.; Ceder, G. Formation enthalpies by mixing GGA and GGA+ U calculations. *Phys. Rev. B* **2011**, *84*, 045115.

(11) Das, H.; Urban, A.; Huang, W.; Ceder, G. First-Principles Simulation of the (Li−−Ni−−Vacancy)O Phase Diagram and Its Relevance for the Surface Phases in Ni-Rich Li-Ion Cathode Materials. *Chem. Mater.* **2017**, *29*, 7840–7851.

(12) Sun, J.; Ruzsinszky, A.; Perdew, J. P. Strongly constrained and appropriately normed semilocal density functional. *Phys. Rev. Lett.* **2015**, *115*, 036402.

(13) Sun, J.; Remsing, R. C.; Zhang, Y.; Sun, Z.; Ruzsinszky, A.; Peng, H.; Yang, Z.; Paul, A.; Waghmare, U.; Wu, X.; Klein, M. L.; Perdew, J. P. Accurate first-principles structures and energies of diversely bonded systems from an efficient density functional. *Nat. Chem.* **2016**, *8*, 831.

(14) Peng, H.; Yang, Z.-H.; Perdew, J. P.; Sun, J. Versatile van der Waals density functional based on a meta-generalized gradient approximation. *Phys. Rev. X* **2016**, *6*, 041005.

(15) Sanchez, J. M.; Ducastelle, F.; Gratias, D. Generalized cluster description of multicomponent systems. *Phys. A: Stat. Mech. Appl.* **1984**, *128*, 334–350.

(16) van de Walle, A.; Ceder, G. Automating first-principles phase diagram calculations. *J. Phase Equilibria* **2002**, *23*, 348–359.

(17) Puchala, B.; Van der Ven, A. Thermodynamics of the Zr−O system from first-principles calculations. *Phys. Rev. B* **2013**, *88*, 094108.

(18) Nelson, L. J.; Hart, G. L.; Zhou, F.; Ozoliņš, V. Compressive sensing as a paradigm for building physics models. *Phys. Rev. B* **2013**, *87*, 035125.

(19) Huang, W.; Urban, A.; Rong, Z.; Ding, Z.; Luo, C.; Ceder, G. Construction of ground-state preserving sparse lattice models for predictive materials simulations. *npj Computational Materials* **2017**, *3*, 30.

(20) Van der Ven, A.; Ceder, G. Lithium diffusion in layered Li_xCoO_2. *Electrochem. Solid-State Lett.* **2000**, *3*, 301.

(21) Van der Ven, A.; Ceder, G.; Asta, M.; Tepesch, P. First-principles theory of ionic diffusion with nondilute carriers. *Phys. Rev. B* **2001**, *64*, 184307.

(22) Van der Ven, A.; Ceder, G. Lithium diffusion mechanisms in layered intercalation compounds. *J. Power Sources* **2001**, *97*, 529–531.

(23) Evans, M.; Polanyi, M. Inertia and driving force of chemical reactions. *Trans. Faraday Soc.* **1938**, *34*, 11–24.

(24) Bronsted, J. Acid and Basic Catalysis. *Chem. Rev.* **1928**, *5*, 231–338.

(25) Bligaard, T.; Nørskov, J. K.; Dahl, S.; Matthiesen, J.; Christensen, C. H.; Sehested, J. The Brønsted–Evans–Polanyi Relation and the Volcano Curve in Heterogeneous Catalysis. *J. Catal.* **2004**, *224*, 206–217.

(26) Li, L.; Li, X.; Duan, Z.; Meyer, R. J.; Carr, R.; Raman, S.; Koziol, L.; Henkelman, G. Adaptive kinetic Monte Carlo simulations of surface segregation in PdAu nanoparticles. *Nanoscale* **2019**, *11*, 10524–10535.

(27) Henkelman, G.; Jónsson, H. Improved tangent estimate in the nudged elastic band method for finding minimum energy paths and saddle points. *J. Chem. Phys.* **2000**, *113*, 9978–9985.

(28) Henkelman, G.; Uberuaga, B. P.; Jónsson, H. A climbing image nudged elastic band method for finding saddle points and minimum energy paths. *J. Chem. Phys.* **2000**, *113*, 9901–9904.

(29) Xiao, P.; Shi, T.; Huang, W.; Ceder, G. Understanding surface densified phases in Ni-rich layered compounds. *ACS Energy Lett.* **2019**, *4*, 811–818.